

Supplementary Information

Rapidly synthesizing gold-palladium core-shell aerogels for selective and robust electrochemical CO₂ reduction

Ran Du, Wei Jin, Hengbo Wu, René Hübner, Lin Zhou, Geng Xue, Yue Hu, and

Alexander

Eychmüller

Experimental Procedures

Reagents and Materials

Reagents including hydrogen tetrachloroaurate (III) ($\text{HAuCl}_4 \cdot 3\text{H}_2\text{O}$), potassium tetrachloropalladate (II) (K_2PdCl_4), polyvinylpyrrolidone (PVP, $M_w = 58000$), and sodium borohydride (NaBH_4), and palladium black were purchased from Sigma-Aldrich, Alfa-Aesar, or Alladin. All reagents were used without further purification.

Fabrication of Noble Metal Aerogels

Au-Pd and Pd hydrogels were synthesized by a NH_4F -induced gelation method.

For the Au-Pd-mix hydrogel (denoted as Au-Pd-mix), $\text{HAuCl}_4 \cdot 3\text{H}_2\text{O}$ solution (32.5 mM, 2.46 mL), K_2PdCl_4 solution (32.5 mM, 2.46 mL), and NaBH_4 aqueous solution (200 mM, 3.2 mL) were successively added into 780 mL water under stirring for 2 min (500–600 rpm). The molar ratio of the metal salt (M), ligand (L), and reductant (R) was 1/10/4. Then, NH_4F (10.0 M, 8 mL) was added into the as-prepared Au-Pt NP solution followed by stirring for ~ 3 min to accelerate the gelation process. Finally, the as-formed aggregates were assembled to yield the Au-Pd-mix hydrogels. The Pd hydrogel was prepared as a similar way, except that $\text{HAuCl}_4 \cdot 3\text{H}_2\text{O}$ solution was replaced with a same amount of K_2PdCl_4 solution.

For the Au-Pd core-shell-structured hydrogel (denoted as Au-Pd-CS- x , x represents the grounding time before adding the second metal salt), a dynamic shelling approach (DSA) was adopted. Briefly, $\text{HAuCl}_4 \cdot 3\text{H}_2\text{O}$ solution (32.5 mM, 2.46 mL) and NaBH_4 aqueous solution (200 mM, 3.2 mL) were successively added into 780 mL water under stirring. Then, NH_4F (10.0 M, 8 mL) was added into the as-formed Au NP solution to induce the gelation process. After stirring for ~ 10 s, the system was kept still. After x min, K_2PdCl_4 solution (32.5 mM, 2.46 mL) was added, and the mixture was stirred for ~ 3 min to accelerate the reaction. Finally, the as-formed aggregates were manually assembled to yield the Au-Pd-CS- x hydrogel.

For the Au hydrogel, $\text{HAuCl}_4 \cdot 3\text{H}_2\text{O}$ solution (32.5 mM, 4.92 mL), PVP (0.4 M, 4.0 mL) were successively added into 775 mL water under stirring for ~ 5 min. Then NaBH_4 aqueous solution (1.0 M, 16 mL) was added and stirred for 20 s before grounding for ~ 24 h to yield the self-supported Au hydrogel.

The resulting hydrogels were purified with water for 4–5 times and then solvent-exchanged with tert-butanol for 2–3 times. Afterwards, the wet gels were flash-frozen by liquid nitrogen (-196 °C) and remained for ~ 5 min to enable complete freezing. The frozen samples were put into the chamber of a freeze dryer (TOPTI-12S-80) and dried for 12–24 h at ~ 1 Pa. The temperature of the cold trap was set to -80 °C.

Computational Procedures

The first principle DFT calculations were performed by the Vienna *Ab initio* Simulation Package (VASP)^[1] with the projector augmented wave (PAW) method^[2]. The exchange functional was treated using the generalized gradient approximation (GGA) of the Perdew-Burke-Ernzerhof (PBE) functional.^[3] The energy cutoff for the plane wave basis expansion was set to 450 eV, and the force on each atom of less than 0.03 eV Å⁻¹ was set as convergence criterion of geometry relaxation. A three-layer 2×3 Au supercell was constructed, where the top-layer was replaced with Pd to simulate the surface of the Au-Pd core-shell aerogel. For the surface of the Au-Pd-mix aerogel, all atoms were randomly distributed with an equal number of Au and Pd atoms. To reveal the potential effect of PdH, a core-shell Au-Pd with PdH outer layer (the Pd layer was replaced by a bilayer containing one Pd layer and one H layer) was modeled (**Figure S17**). To qualitatively explore the effect of valence states at the aerogel surface, the model of the core-shell-structured Au-Pd aerogel was slightly modified, where an oxygen atom was bonded to a surface Pd atom (see **Figure S18**). For all models, the bottom layer was fixed during geometric relaxation. The Brillouin-zone integration was sampled by single Γ point. The self-consistent calculations applied a convergence energy threshold of 10⁻⁴ eV.

In this work, the CO₂ reduction path was considered as followed:



Here, the asterisk (*) represents the surface-active site. The free energies of the CO₂ reduction steps were calculated by the equation^[4]: $\Delta G = \Delta E_{\text{DFT}} + \Delta E_{\text{ZPE}} - T\Delta S$, where ΔE_{DFT} is the DFT electronic energy difference of each step; ΔE_{ZPE} and ΔS are the correction of the zero-point energy and the variation of entropy, respectively, which were obtained by vibration analysis; T is the temperature ($T = 300$ K).

Characterizations

Microscopy Characterization

Scanning electron microscopy (SEM) analysis was performed on a Nova 200 NanoSEM scanning electron microscope operated at 1 kV. Samples were prepared by directly sticking on conductive tape.

Transmission electron microscopy (TEM) analysis was carried out by using a FEI Tecnai G20 microscope or a JEOL JEM-2100F microscope operated at 200 kV. Samples were prepared by dispersing in acetone under ultrasonication (15 s to 120 s, depending on their dispersing ability), followed by dropping onto carbon-coated copper grids and drying at ambient temperature.

High-resolution TEM imaging was done at an image- C_s -corrected Titan 80-300 microscope (FEI) operated at an accelerating voltage of 300 kV. High-angle annular dark-field scanning transmission electron microscopy (HAADF-STEM) imaging combined with spectrum imaging analysis based on energy-dispersive x-ray spectroscopy (EDX) were performed at 200 kV with a Talos F200X microscope equipped with an X-FEG electron source and a Super-X EDX detector system (FEI). Prior to (S)TEM analysis, the specimen mounted in a high-visibility low-background holder was placed for 2 s into a Model 1020 Plasma Cleaner (Fischione) to remove possible contaminations.

Diffraction Characterization

X-ray powder diffraction (XRD) was carried out on a D8 Advance X-ray diffractometer (Bruker) with Cu K α radiation ($\lambda = 1.54178 \text{ \AA}$).

Element Analysis

X-Ray photoelectron spectroscopy (XPS) was performed by an X-ray photoelectron spectrometer (Thermo Kalphaa, Kratos, UK) with a monochromatic Al source. The XPS spectra were taken after all binding energies were referenced to the C 1s neutral carbon peak at 284.8 eV.

Inductively coupled plasma atomic emission spectroscopy (ICP-AES) was performed using an Agilent 720ES optical emission spectrometer.

Gas Adsorption Measurement

Nitrogen adsorption experiments were performed with ASAP 2020 (Micromeritics) at 77 K. Before the measurements, the samples were outgassed at 323 K for ~24 h under vacuum. A filling rod was used to reduce the dead volume, thus improving the measurement accuracy. The specific surface area was calculated by using the multi-point BET equation ($0.1 < p/p_0 < 0.3$). The total pore volume was calculated at $p/p_0 = 0.99$.

Electrochemical Measurements

All electrochemical tests were performed on a CHI 660E electrochemical analyzer. An airtight two-compartment electrochemical cell filled with 0.1 M KHCO₃ electrolyte (pH 6.8) in each chamber was used, where the two compartments were separated by an anion exchange membrane. Furthermore, a standard three-electrode system was applied, including a glassy carbon (5 mm in diameter) electrode as working electrode, an Ag/AgCl electrode (saturated with 3.0 M KCl aqueous solution) as reference electrode, and a platinum foil as counter electrode. Each ink was prepared by mixing 2 mg of catalyst, 20 μL of 5 wt% Nafion solution, and 180 μL of isopropanol followed by ultrasonication. A 20 μL aliquot of the carbon ink was dropped on the glassy carbon electrode, yielding the working electrode. The working and counter electrodes were respectively placed in the two compartments of the electrochemical cell.

All potentials were converted to the reversible hydrogen electrode (RHE) by using the following equation:

$$E_{\text{RHE}} = E_{\text{Ag/AgCl}} + 0.197 \text{ V} + 0.059 \times \text{pH}$$

Before electrocatalysis, the cathodic compartment was bubbled with CO₂ gas for 30 min. A steady supply of CO₂ gas was delivered at a rate of 20.0 sccm. Before the test, the working electrode was activated by cycling between 0 and -0.7 V for ~100 cycles at 50 mV s⁻¹. During the tests, the cathode compartment was vented directly into the sampling loop of a gas chromatography system (Agilent 7890B) to analyze the generated gases. The liquid products were analyzed by the nuclear magnetic resonance technique. The Faradaic efficiency (*FE*) and mass activity for CO generation (*J_m*) were calculated as follows^[5-6]:

$$FE = eF \times n / Q$$

$$J_m = FE_{\text{CO}} \times I / m_{\text{Au+Pd}}$$

where *e* is the number of electrons transferred for the specific product, *Q* is the total charge, *n* is the molar amount of different products, *F* is the Faraday constant, *I* is measured current, and *m_{Au+Pd}* is the weight of metals in the catalyst.

The electrochemical double layer capacitance was calculated from cyclic voltammetry (CV) curves with scan rates of 20–160 mV s⁻¹. Electrochemical impedance spectroscopy (EIS) was performed with frequencies ranging from 0.1 MHz to 1 Hz with an amplitude of 5 mV at open-circuit voltage.

Figures



Figure S1. Photograph of an Au-Pd-CS-2min aerogel.

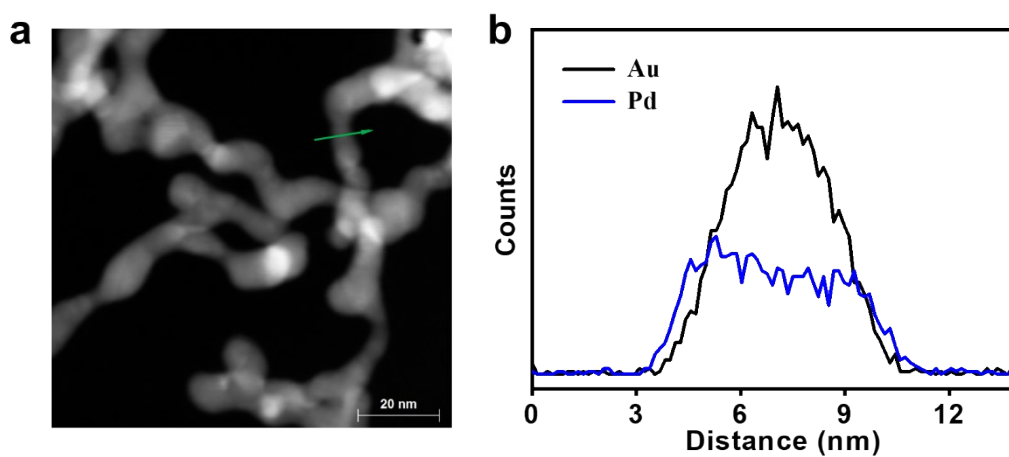


Figure S2. (a) HAADF-STEM image of the Au-Pd-CS-2min aerogel and (b) the line scan for the position indicated by a green arrow.

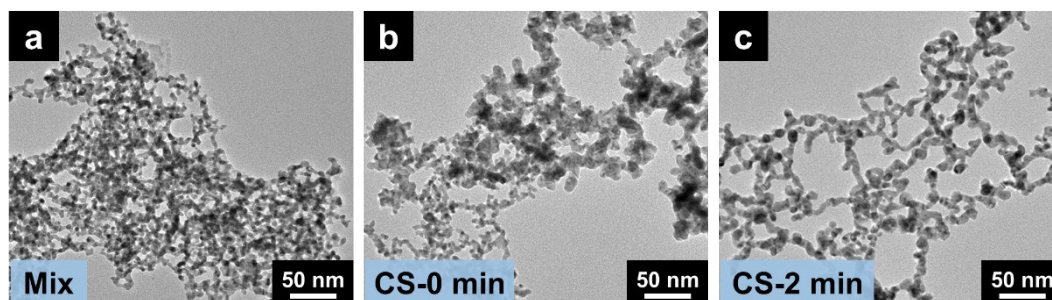


Figure S3. Representative TEM images of the indicated Au-Pd aerogels.

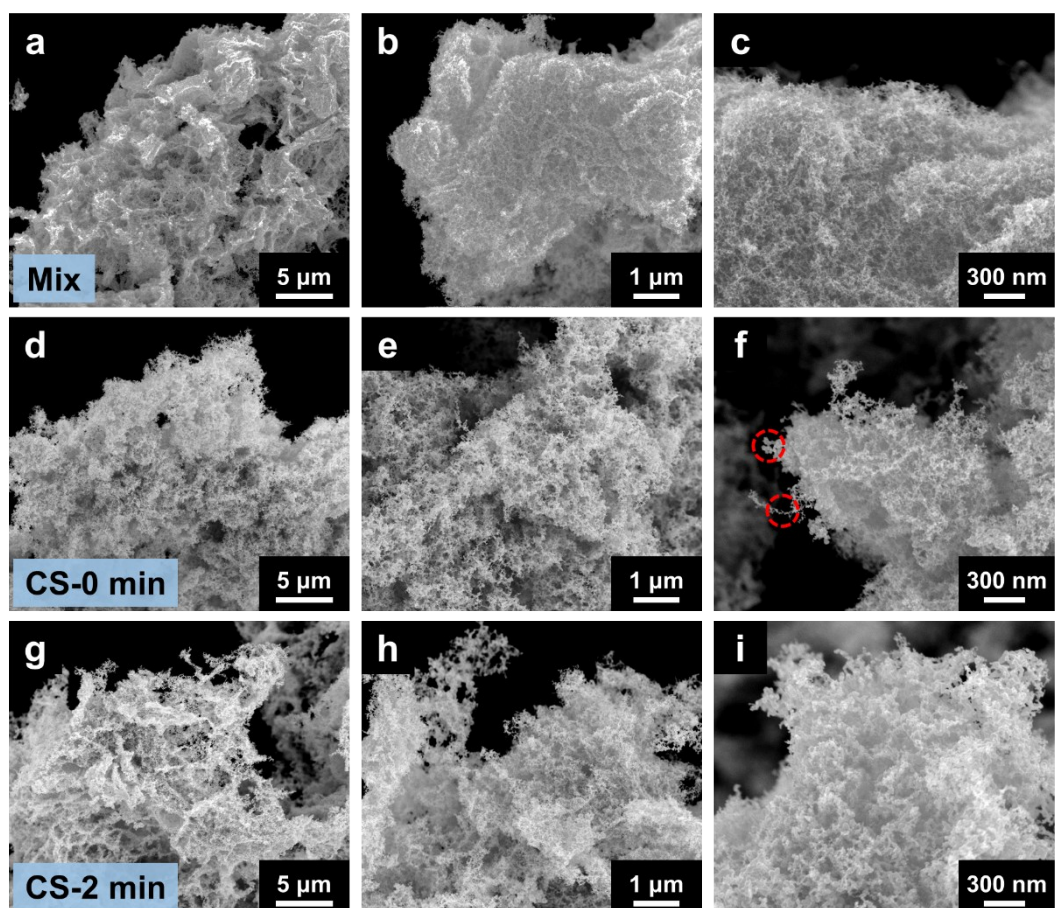


Figure S4. Representative SEM images of the indicated Au-Pd aerogels at different magnifications. Inhomogeneous ligaments of the Au-Pd-CS-0 min aerogel are circled in panel f.

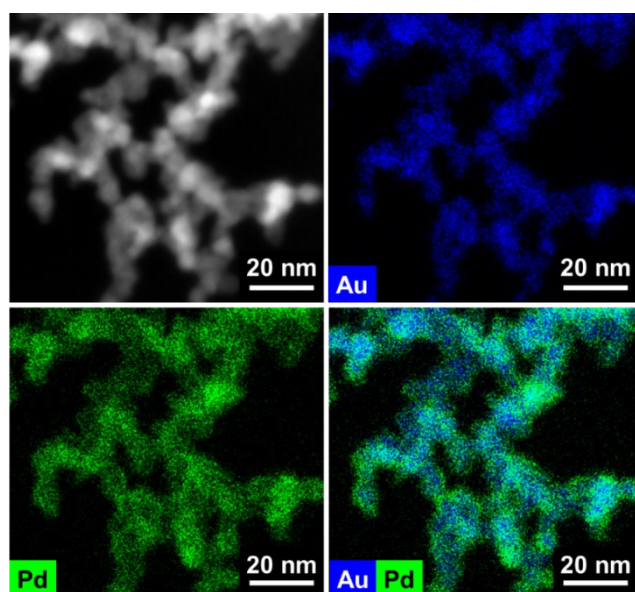


Figure S5. HAADF-STEM image and the corresponding EDX-based element distributions for the Au-Pd-mix aerogel.

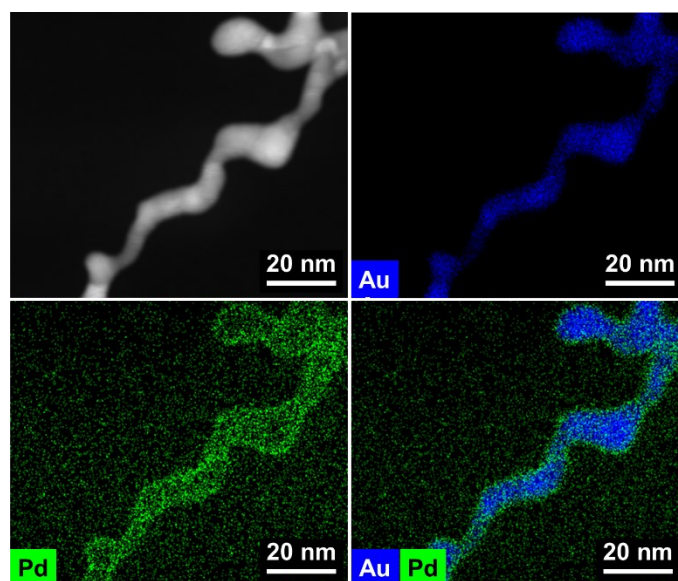


Figure S6. HAADF-STEM image and the corresponding EDX-based element distributions for the Au-Pd-CS-0 min aerogel.

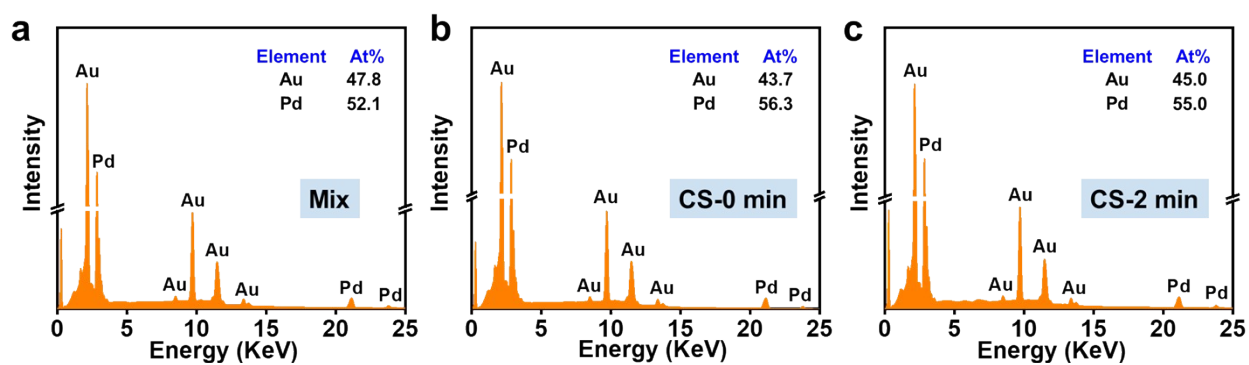


Figure S7. Elemental analysis of the indicated aerogels by using TEM-EDX.

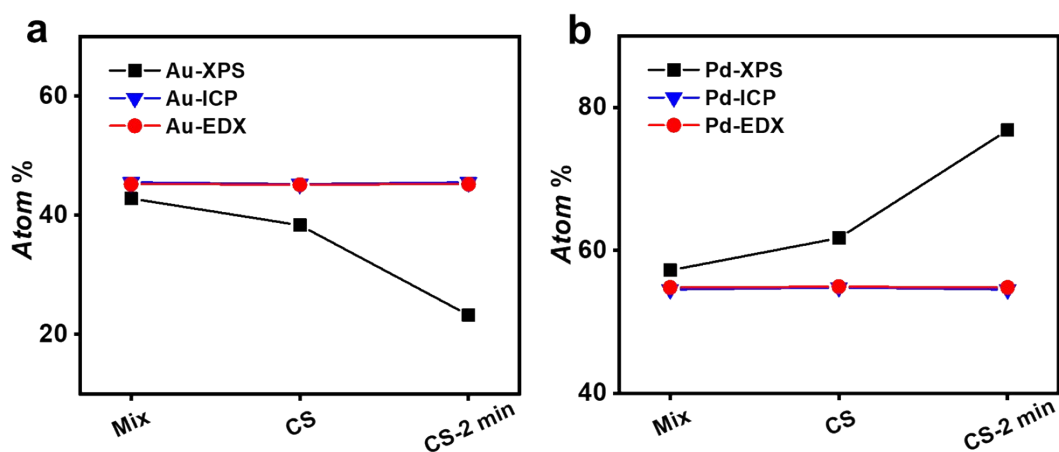


Figure S8. Comparison of the (a) gold and (b) palladium fraction of the indicated aerogels as characterized by XPS, ICP-AES, and TEM-EDX.

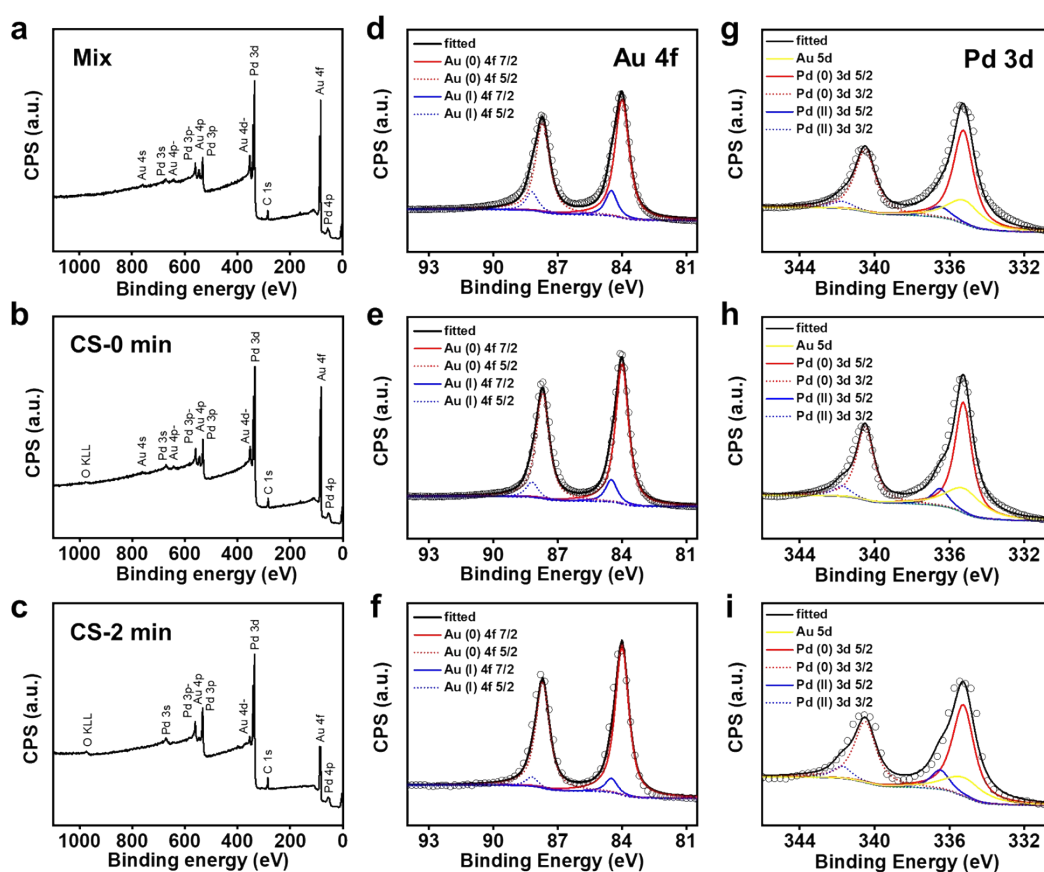


Figure S9. (a-c) Full XPS spectra, (d-f) high-resolution gold spectra, and (g-i) high-resolution palladium spectra of the indicated aerogels.

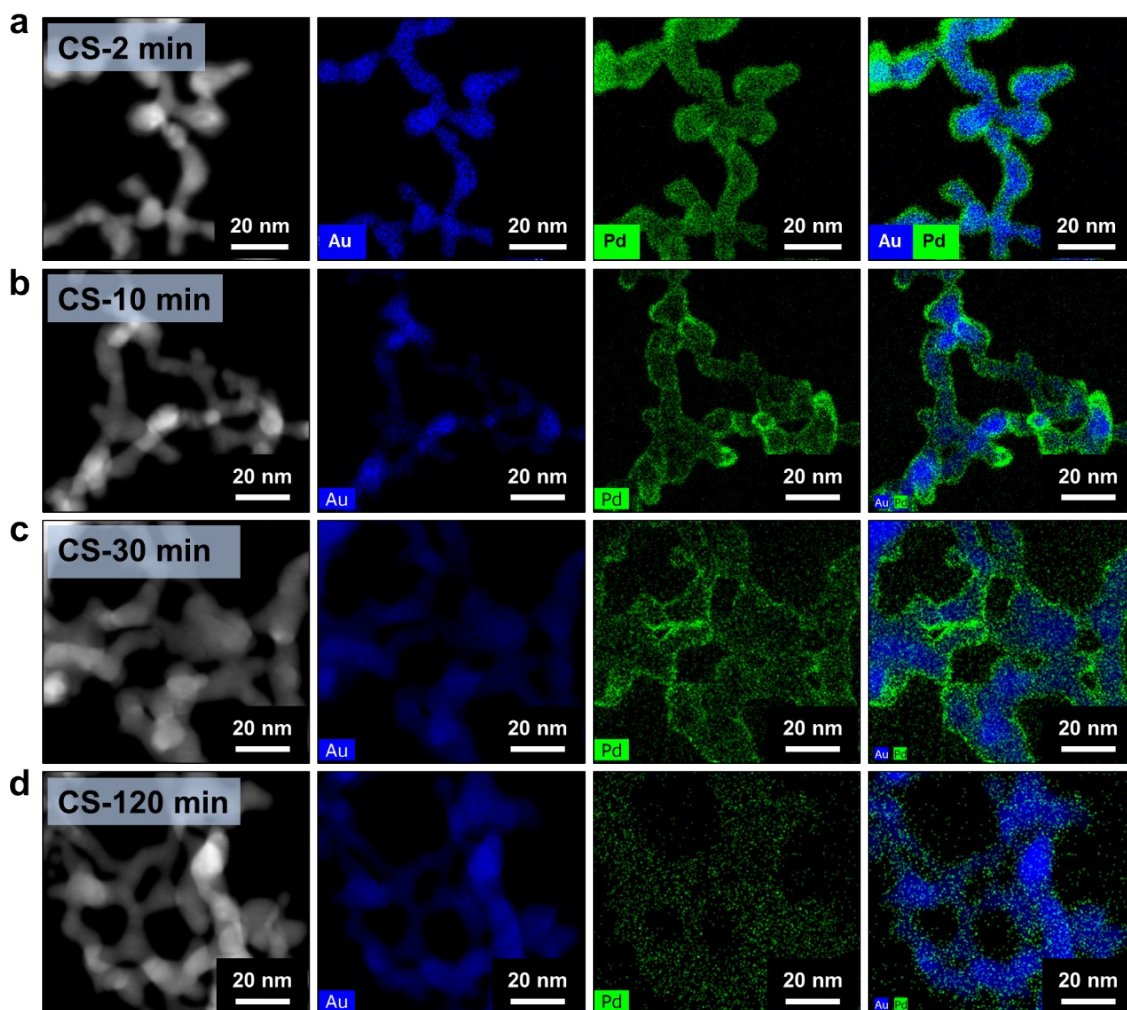


Figure S10. HAADF-STEM images and the corresponding EDX-based element distributions of the indicated Au-Pd-CS-*x* aerogels.

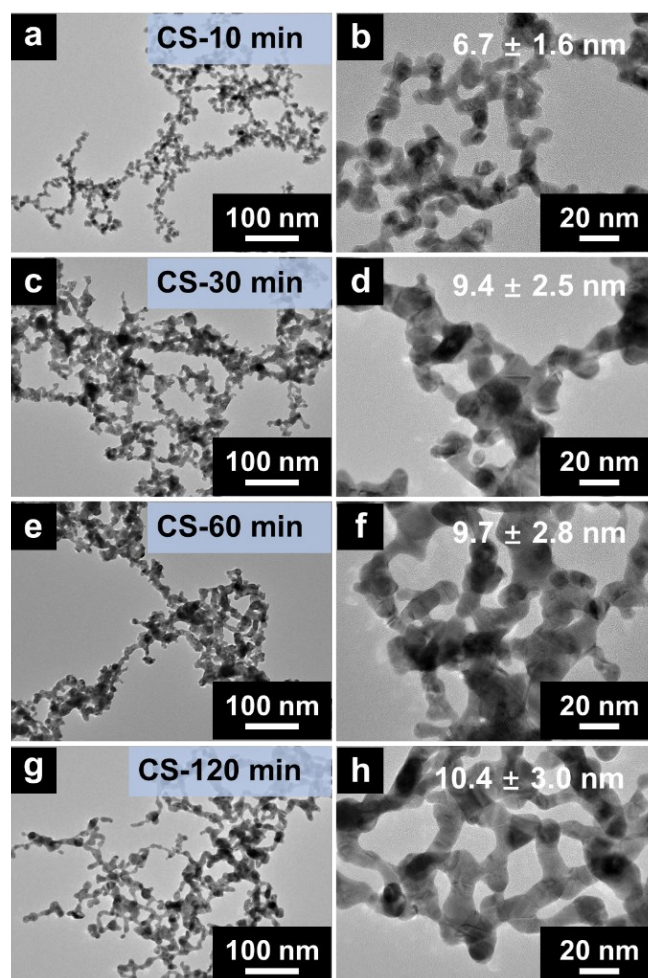


Figure S11. TEM images of the indicated Au-Pd-CS-*x* aerogels.

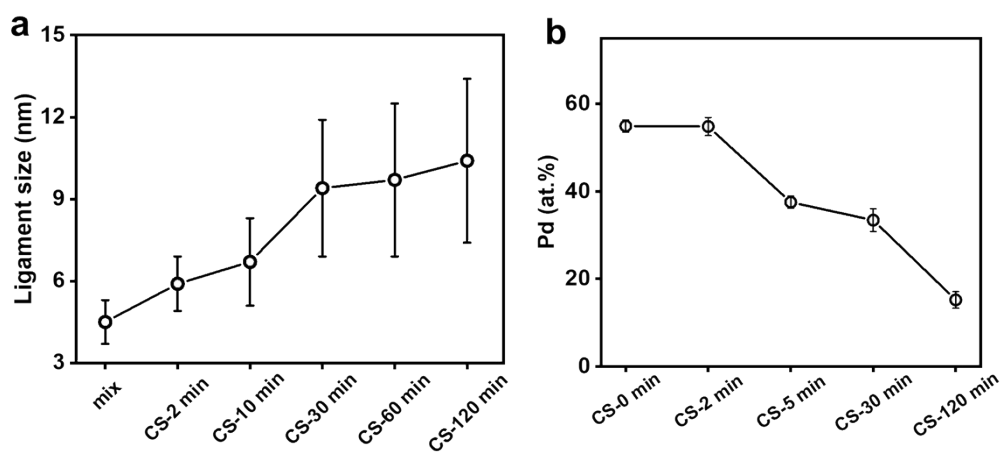


Figure S12. Plots of (a) ligament size and (b) Pd content (from TEM-EDX analysis) for the indicated aerogels.

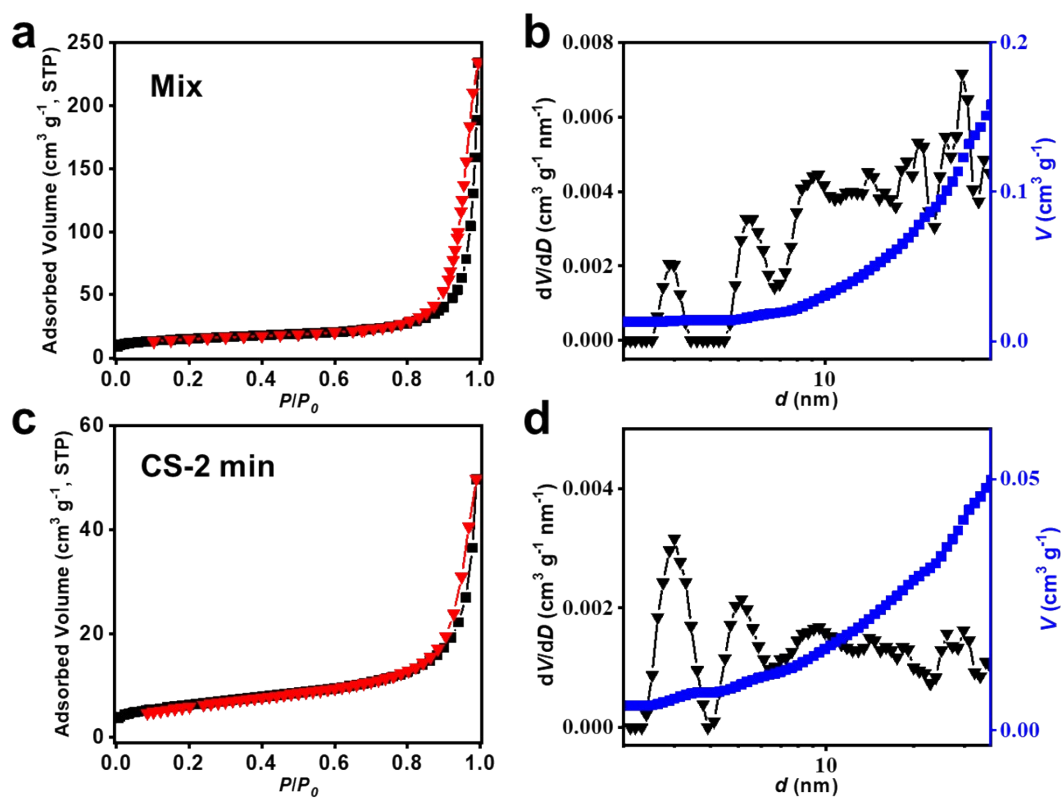


Figure S13. Nitrogen adsorption isotherms and the corresponding pore size distributions obtained by the NLDFT method for the indicated aerogels. The specific surface area and the pore volume are 53.9 m² g⁻¹ and 0.29 cm³ g⁻¹ for Au-Pd-mix and are 21.9 m² g⁻¹ and 0.08 cm³ g⁻¹ for Au-Pd-CS-2 min.

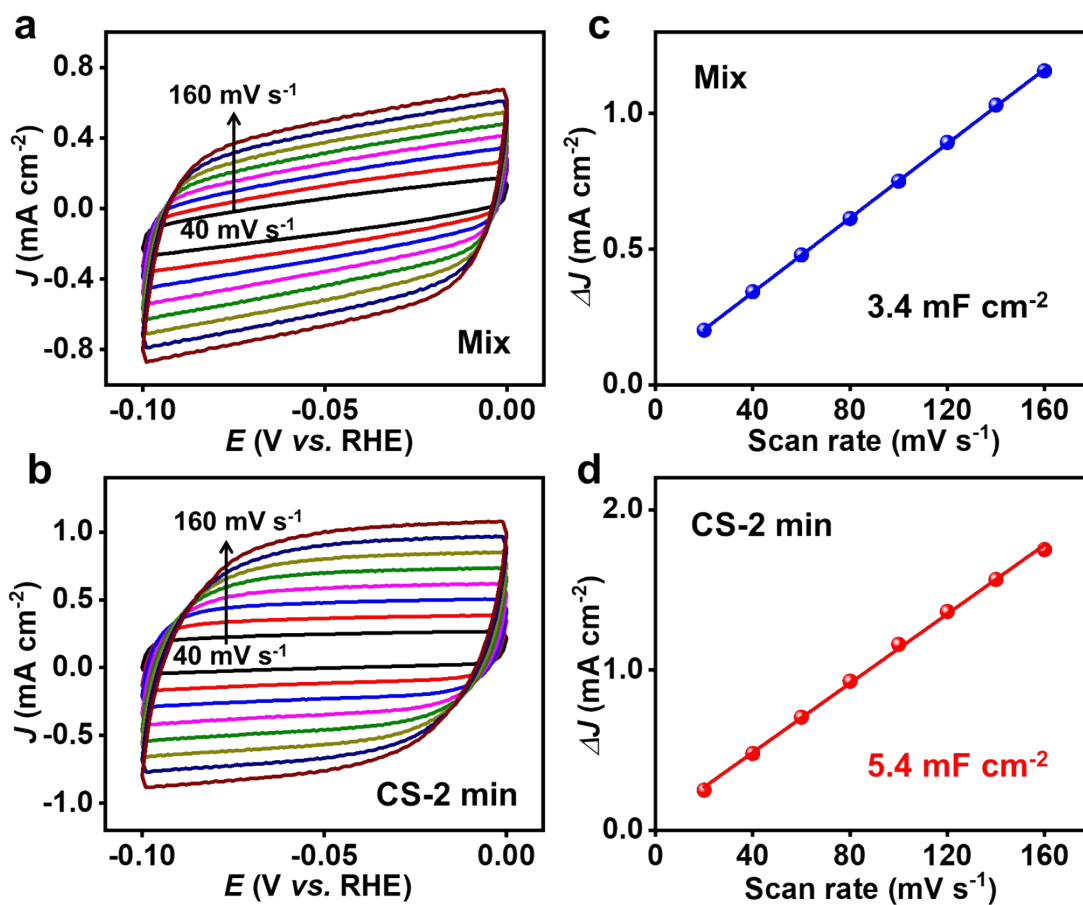


Figure S14. (a-b) CV curves and (c-d) linear fitting of capacitive current densities vs. scan rates of the Au-Pd-mix and Au-Pd-CS-2 min aerogels.

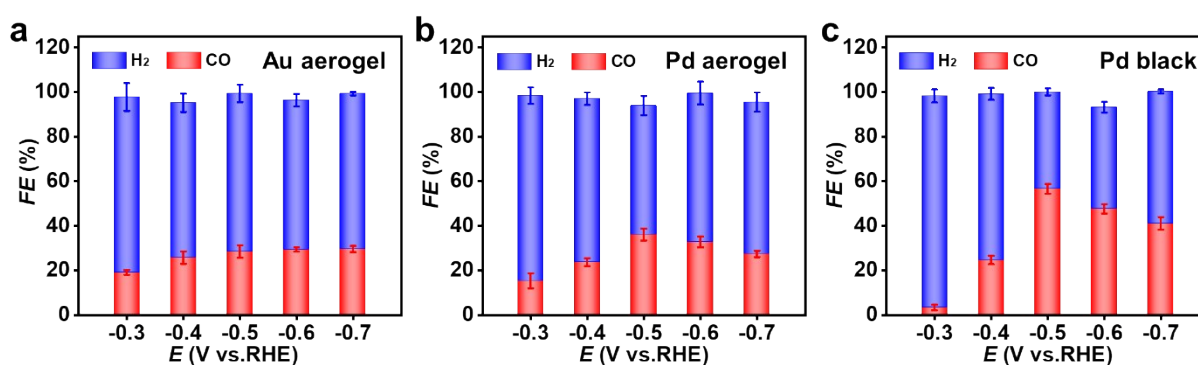


Figure S15. Faradaic efficiencies of CO and H₂ for the (a) Au aerogels, (b) Pd aerogels, and (c) Pd black.

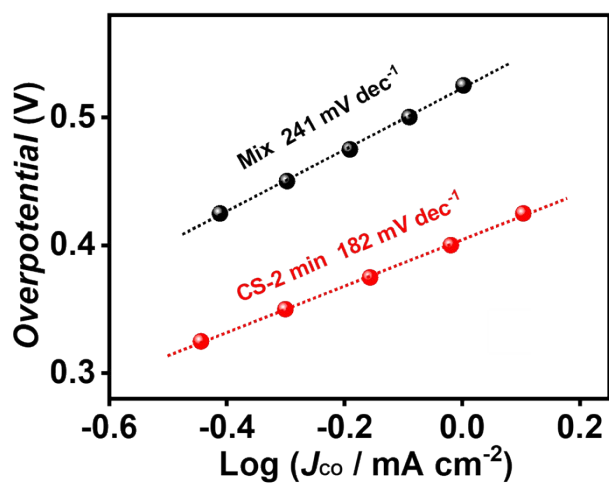


Figure S16. Tafel plots of the partial CO current density for the indicated Au-Pd aerogels.

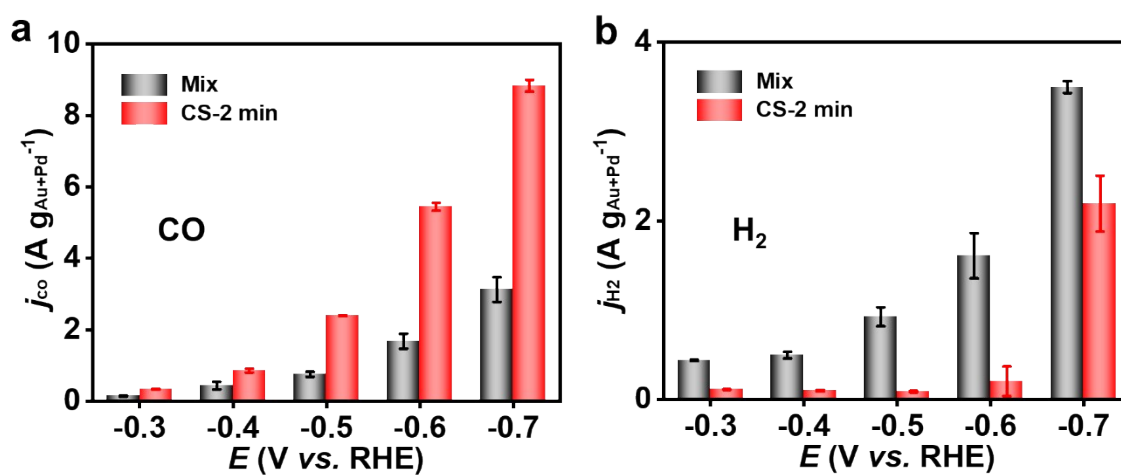


Figure S17. Mass activities of (a) CO and (b) H₂ for the Au-Pd-mix and Au-Pd-CS-2 min aerogels at different applied potentials.

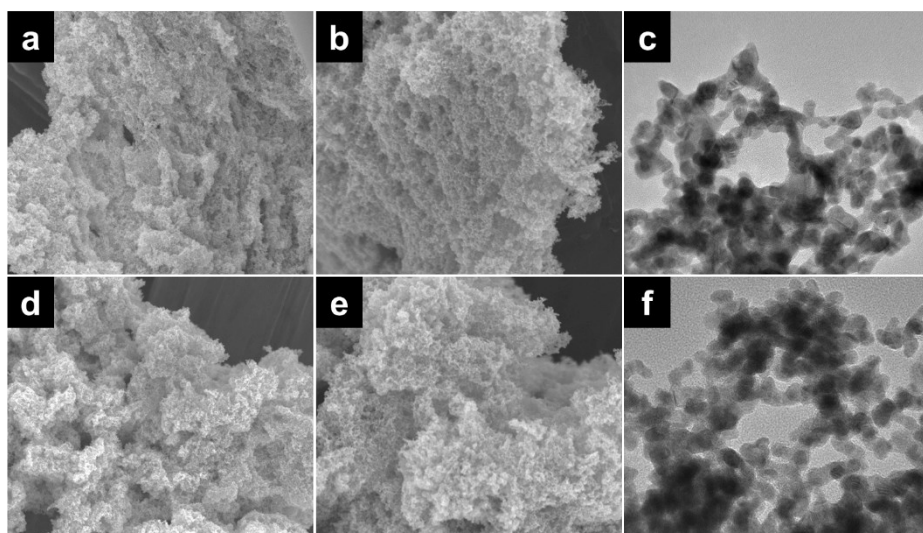


Figure S18. (a,b,d,e) SEM images and (c,f) TEM images of the Au-Pd-CS-2 min before (a-c) and after (d-f) operating for electrocatalytic CO₂ reduction for 12 hours. Note that the samples are prepared on carbon paper with Nafion, hence the morphologies may not be the same as those for the pristine aerogels.

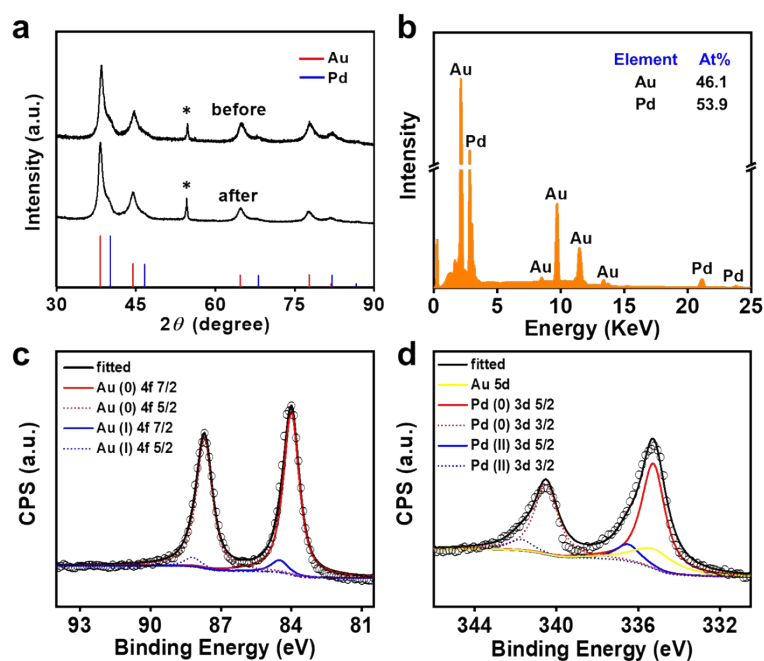


Figure S19. Characterizations of Au-Pd-CS-2 min before and after operating for electrocatalytic CO₂ reduction for 12 hours. (a) XRD of Au-Pd-CS-2 min based electrode on carbon paper before and after operation. The asterisks indicate the peak of the carbon paper. (b) EDX of the Au-Pd-CS-2 min after operation. (c-d) High-resolution of the gold and palladium XPS spectra of Au-Pd-CS-2 min after operation.

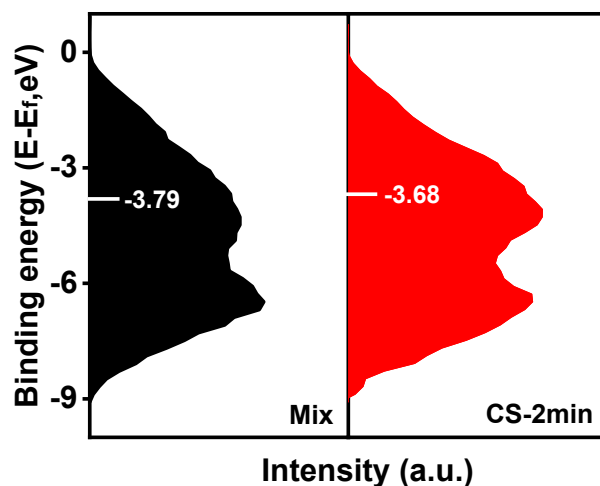


Figure S20. Valence-band XPS spectra of the Au-Pd-mix and Au-Pd-CS-2 min aerogels. The white bars indicate the center of gravity.

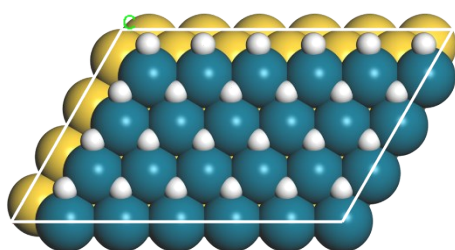


Figure S21. Model of a core-shell Au-Pd with PdH outer layer (*i.e.*, CS-PdH model). Yellow balls, dark-blue, and white balls represent Au, Pd, and H atoms, respectively.

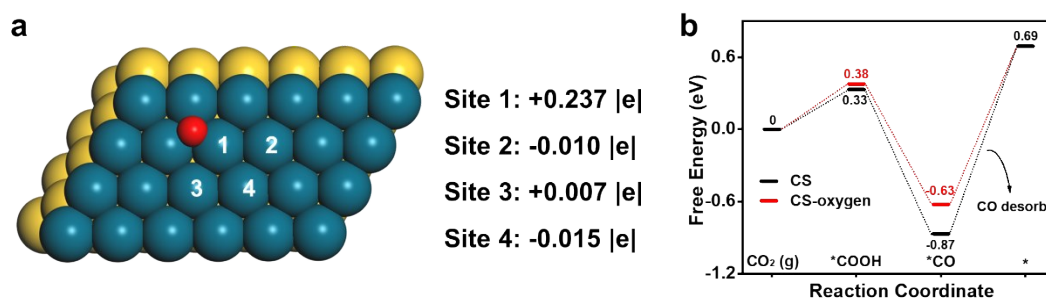


Figure S22. Model of a core-shell Au-Pd bonded with a surface oxygen atom (*i.e.*, CS-oxygen model). The charge of palladium atoms at different sites with respect to the oxygen is listed on the right-hand side. (b) Free-energy diagrams of CO₂RR on the Au-Pd with core-shell model and core-shell-oxygen model.

Tables

Table S1. Element analysis of different Au-Pd aerogels (atomic ratio of Au/Pd).

	Au-Pd	Au-Pd-CS-0 min	Au-Pd-CS-2 min
XPS	42.8 / 57.2	38.3 / 61.7	23.2 / 76.8
ICP-OES	45.5 / 54.5	45.2 / 54.8	45.5 / 54.5
EDX with TEM	47.9 / 52.1	43.7 / 56.3	45.2 / 54.8

Table S2. Valence state analysis of the different Au-Pd aerogels from the corresponding XPS spectra. The deconvolution of the high-resolution XPS spectra gives rise to Au (0) 4f 7/2 (84.0 eV), Au (I) 4f 7/2 (84.5 eV), Pd (0) 3d 5/2 (335.3 eV), and Pd (II) 3d 5/2 (336.5 eV), respectively.

	Au / at. %		Pd / at. %	
Au-Pd-mix	Au (0) 4f	84.9	Pd (0) 3d	89.2
	Au (I) 4f	15.1	Pd (II) 3d	10.8
Au-Pd-CS-0 min	Au (0) 4f	88.0	Pd (0) 3d	86.9
	Au (I) 4f	12.0	Pd (II) 3d	13.1
Au-Pd-CS-2 min	Au (0) 4f	92.6	Pd (0) 3d	84.7
	Au (I) 4f	7.3	Pd (II) 3d	15.3
Au-Pd-CS-2 min after electrocatalysis	Au (0) 4f	92.8	Pd (0) 3d	85.3
	Au (I) 4f	7.2	Pd (II) 3d	14.7

Table S3. Comparison of the Faradaic efficiency (*FE*) for CO conversion with different noble-metal-based CO₂RR electrocatalysts.

Catalysts	Electrolyte	Mass loading (mg/cm ²)	<i>E</i> (V vs. RHE)	<i>FE</i> _{CO} (%)	Ref.
Au-Pd-CS-2 min	0.1 M KHCO₃	1	-0.6	99.96	this work
Au-Pd-mix	0.1 M KHCO₃	1	-0.5	42.10	this work
N-heterocyclic carbene-functionalized Au nanocluster ^a	0.5 M KHCO ₃	0.25	-1	> 80	[7]
8 nm Au NPs ^{ab}	0.5 M KHCO ₃	/	-0.67	90	[8]
Oxide-derived Au NPs	0.5 M NaHCO ₃	/	-0.35	> 96	[9]
Ultrathin Au nanowires ^{ab}	0.5 M KHCO ₃	/	-0.35	94	[10]
Nanoporous Au	0.05 M K ₂ CO ₃	/	-0.5	90-99	[11]
Nanoporous Au	0.5 M K ₂ CO ₃	/	-0.6	94	[12]
porous Au films	0.1 M KHCO ₃	/	-0.5	90.5	[13]
Au (110)	0.1 M KHCO ₃	/	-0.74	79	[14]
AuCu ₃ @Au	0.1 M KHCO ₃	/	-0.6	97.27	[15]
3.7 nm Pd NPs ^{ab}	0.1 M KHCO ₃	0.4	-0.89	91.2	[16]
Octahedral Pd NPs ^c	0.5 M NaHCO ₃	3	-0.9	92	[17]
Pd nanosheets ^b	0.1 M KHCO ₃	0.1	-0.5	94	[18]
Pd–Au nanowires	0.5 M KHCO ₃	0.115	-0.6	94.3	[19]
Ag nanofoam	0.5 M KHCO ₃	1.45	-0.6	96.72	[20]
Nanostructured Ag	0.1 M KHCO ₃	N/A	-0.4	92	[21]
5 nm Ag/C ^b	0.5 M KHCO ₃	0.09	-0.75	~80	[22]

^a The catalyst is prepared on the carbon paper.

^b Carbon additives have been involved.

^c The catalyst is prepared on the gas diffusion layer electrode.

References

- [1] G. Kresse, J. Furthmüller, *Comput. Mater. Sci* **1996**, *6*, 15-50.
- [2] P. E. Blöchl, *Phys. Rev. B* **1994**, *50*, 17953-17979.
- [3] J. P. Perdew, J. A. Chevary, S. H. Vosko, K. A. Jackson, M. R. Pederson, D. J. Singh, C. Fiolhais, *Phys. Rev. B* **1992**, *46*, 6671-6687.
- [4] E. Skúlason, T. Bligaard, S. Gudmundsdóttir, F. Studt, J. Rossmeisl, F. Abild-Pedersen, T. Vegge, H. Jónsson, J. K. Nørskov, *Phys. Chem. Chem. Phys.* **2012**, *14*, 1235-1245.
- [5] S. Nellaiappan, N. K. Katiyar, R. Kumar, A. Parui, K. D. Malviya, K. G. Pradeep, A. K. Singh, S. Sharma, C. S. Tiwary, K. Biswas, *ACS Catal.* **2020**, *10*, 3658-3663.
- [6] K. Sun, T. Cheng, L. Wu, Y. Hu, J. Zhou, A. Maclennan, Z. Jiang, Y. Gao, W. A. Goddard, Z. Wang, *J. Am. Chem. Soc.* **2017**, *139*, 15608-15611.
- [7] M. R. Narouz, K. M. Osten, P. J. Unsworth, R. W. Y. Man, K. Salorinne, S. Takano, R. Tomihara, S. Kaappa, S. Malola, C.-T. Dinh, J. D. Padmos, K. Ayoo, P. J. Garrett, M. Nambo, J. H. Horton, E. H. Sargent, H. Häkkinen, T. Tsukuda, C. M. Crudden, *Nat. Chem.* **2019**, *11*, 419-425.
- [8] W. Zhu, R. Michalsky, Ö. Metin, H. Lv, S. Guo, C. J. Wright, X. Sun, A. A. Peterson, S. Sun, *J. Am. Chem. Soc.* **2013**, *135*, 16833-16836.
- [9] Y. Chen, C. W. Li, M. W. Kanan, *J. Am. Chem. Soc.* **2012**, *134*, 19969-19972.
- [10] W. Zhu, Y.-J. Zhang, H. Zhang, H. Lv, Q. Li, R. Michalsky, A. A. Peterson, S. Sun, *J. Am. Chem. Soc.* **2014**, *136*, 16132-16135.
- [11] A. J. Welch, J. S. DuChene, G. Tagliabue, A. Davoyan, W.-H. Cheng, H. A. Atwater, *ACS Applied Energy Materials* **2019**, *2*, 164-170.
- [12] W. Zhang, J. He, S. Liu, W. Niu, P. Liu, Y. Zhao, F. Pang, W. Xi, M. Chen, W. Zhang, S.-S. Pang, Y. Ding, *Nanoscale* **2018**, *10*, 8372-8376.
- [13] C. Chen, B. Zhang, J. Zhong, Z. Cheng, *J. Mater. Chem. A* **2017**, *5*, 21955-21964.
- [14] N. Todoroki, H. Tei, H. Tsurumaki, T. Miyakawa, T. Inoue, T. Wadayama, *ACS Catal.* **2019**, *9*, 1383-1388.
- [15] X. Ma, Y. Shen, S. Yao, C. An, W. Zhang, J. Zhu, R. Si, C. Guo, C. An, *J. Mater. Chem. A* **2020**, *8*, 3344-3350.
- [16] D. Gao, H. Zhou, J. Wang, S. Miao, F. Yang, G. Wang, J. Wang, X. Bao, *J. Am. Chem. Soc.* **2015**, *137*, 4288-4291.
- [17] W. Zhu, S. Kattel, F. Jiao, J. G. Chen, *Adv. Energy Mater.* **2019**, *9*, 1802840.
- [18] W. Zhu, L. Zhang, P. Yang, C. Hu, Z. Luo, X. Chang, Z.-J. Zhao, J. Gong, *Angew. Chem. Int. Ed.* **2018**, *57*, 11544-11548.
- [19] S. Zhu, Q. Wang, X. Qin, M. Gu, R. Tao, B. P. Lee, L. Zhang, Y. Yao, T. Li, M. Shao, *Adv. Energy Mater.* **2018**, *8*, 1802238.
- [20] L. Wei, H. Li, J. Chen, Z. Yuan, Q. Huang, X. Liao, G. Henkelman, Y. Chen, *ACS Catal.* **2020**, *10*, 1444-1453.
- [21] M. Ma, K. Liu, J. Shen, R. Kas, W. A. Smith, *ACS Energy Lett.* **2018**, *3*, 1301-1306.
- [22] C. Kim, H. S. Jeon, T. Eom, M. S. Jee, H. Kim, C. M. Friend, B. K. Min, Y. J. Hwang, *J. Am. Chem. Soc.* **2015**, *137*, 13844-13850.